# High-spatial-resolution 2D shape sensing based on OFDR using adaptive spectrum method with narrow sweep range

RONGYI SHAN,<sup>1,2</sup> CAILING FU,<sup>1,2,\*</sup> D YANJIE MENG,<sup>1,2</sup> D HUAJIAN ZHONG,<sup>1,2</sup> WENFA LIANG,<sup>1,2</sup> SHUAI XIAO,<sup>1,2</sup> YUHAO KONG,<sup>1,2</sup> ZHENWEI PENG,<sup>1,2</sup> WEIJIA BAO,<sup>1,2</sup> YONGZHENG XU,<sup>1,2</sup> AND YIPING WANG<sup>1,2,3</sup> D

**Abstract:** What we believe to be a novel wavelength shift demodulation method for optical frequency domain reflectometry (OFDR), i.e., adaptive spectrum method (ASM), was proposed and demonstrated to achieve high-spatial-resolution two-dimensional (2D) shape sensing with a narrow sweep range. The root-mean-square errors (RMSEs) of strain sections in multicore fiber (MCF) sensing cores with different local reference spectrum lengths and corresponding wavelength ranges were analyzed. Compared with traditional method, the spectral similarity of strain section was significantly improved and the strain distribution of the outer sensing cores was successfully demodulated at a spatial resolution of 2.1 mm by using ASM. Furthermore, the 2D shapes were successfully reconstructed at curvature radii of 20, 25, 30, and 50 mm, respectively. The maximum end position deviation was 6.89 mm for the MCF length of 500 mm, and the average deviation error of each reconstructed section was further analyzed. Ultimately, the ASM was deployed on the graphics processing unit (GPU) to perform parallel computation under the size of zero-padding of 1024, 2048, 4096, and 8192, respectively. Compared to serial computation on the CPU, the time consumption was reduced by a factor of 8.4 under the size of zero padding of 4096 and wavelength gap of 0.00390 nm.

© 2025 Optica Publishing Group under the terms of the Optica Open Access Publishing Agreement

# 1. Introduction

Optical fiber shape sensing based on multicore fiber (MCF) has wide applications in civil structural health monitoring [1,2], aircraft wing shape measurement [3], and minimally invasive procedures [4,5], due to its advantage of compactness, small size, flexibility, and resistance to harsh environments [6]. Several shape sensing technologies based on fiber Bragg gratings [7], phase-sensitive optical time domain reflectometry [8] and Brillouin optical time domain analysis [9] have been proposed and demonstrated. However, the shape sensing ability of the afore-mentioned technologies are limited by cm-level spatial resolution. Recently, shape sensing based on optical frequency domain reflectometry (OFDR) has attracted significant interest owing to its high spatial resolution and high sensitivity [10–12]. The high-precision demodulation of strain distribution in sensing core was a key factor in achieving OFDR shape sensing. However, the random noise and deteriorated similarity of Rayleigh backscattering spectra caused by large strain can lead to high-spatial-resolution strain demodulation failure, i.e., shape reconstruction

#566500 Journal © 2025 https://doi.org/10.1364/OE.566500

<sup>&</sup>lt;sup>1</sup>Shenzhen Key Laboratory of Photonic Devices and Sensing Systems for Internet of Things, Guangdong and Hong Kong Joint Research Centre for Optical Fibre Sensors, State Key Laboratory of Radio Frequency Heterogeneous Integration, Shenzhen University, Shenzhen 518060, China

<sup>&</sup>lt;sup>2</sup>Shenzhen Key Laboratory of Ultrafast Laser Micro/Nano Manufacturing, Key Laboratory of Optoelectronic Devices and Systems of Ministry of Education/Guangdong Province, College of Physics and Optoelectronic Engineering, Shenzhen University, Shenzhen 518060, China

<sup>&</sup>lt;sup>3</sup> Guangdong Laboratory of Artificial Intelligence and Digital Economy (SZ), Shenzhen 518107, China \*fucailing@szu.edu.cn

failure [13,14]. A local spectrum matching method was proposed to efficiently eliminate the cross-correlation fake-peaks and multi-peaks by matching the most similarity portion in the measurement spectrum, achieving a shape reconstruction error of 1 cm along a 1 m sensing fiber under a spatial resolution of 9.5 mm [15]. Subsequently, a phase de-hopping filtering differential phase strain demodulation method was also proposed to remove outliers in shape sensing, which greatly improved the demodulation rate of shape sensing under the spatial resolution of 45  $\mu$ m [16]. A post-processing method using first-order differential local filtering was proposed to suppress fake peaks of the wavelength shift signal to improve the accuracy of shape reconstruction [17]. Therefore, the performance of shape sensing in OFDR could be improved by reducing outliers of strain distribution in the sensing cores.

In this letter, a high-spatial-resolution, i.e., 2.1 mm, two-dimensional (2D) OFDR shape sensor based on MCF was demonstrated using the adaptive spectrum method (ASM) with a narrow sweep range, i.e., 4 nm. The working principle and process of ASM were explained, and the optimal local reference spectrum length and corresponding wavelength range of two external outer cores of MCF, i.e., Core5 and Core6, based on strain root-mean-square error (RMSE) were further analyzed. The normalized similarity and demodulated strain distribution at different curvature radii were also compared using ASM and traditional method (TM). Moreover, the reconstruction error of 2D shapes was further evaluated. Furthermore, the time consumption for CPU serial processing and graphics processing unit (GPU) parallel processing under different sizes of zero padding was compared.

### 2. System setup and operation principle

The experimental setup for 2D shape sensing using OFDR with MCF was depicted in Fig. 1. The light from the tunable laser source (TLS) is split into two parts by an optical coupler ( $OC_1$ ) with a splitting ratio of 10:90, and injected into the auxiliary interferometer (AI) and main interferometer (MI), respectively. In the experiment, the TLS was swept from 1548 to 1552 nm at a sweep velocity of 50 nm/s, corresponding to a wavelength sweep range of 4 nm, i.e.,  $\Delta \lambda = 4$  nm. The AI based on the Michelson interferometer structure consisted of a 51.5-meter-long delay fiber and two Faraday rotating mirrors (FRMs). The AI beat frequency signal collected by the balanced photodetector (BPD<sub>1</sub>) was used as an external trigger signal for data acquisition card (DAQ). The light entering the MI was split into two paths by  $OC_2$ , and injected into the reference arm, i.e., polarization controller (PC), and measurement arm, i.e., MCF, respectively. Note that the employed MCF was the same as that in literature [18], and the length was 50 cm. Then, the light from the reference and measurement arms mixed by OC4 was divided into p- and s-polarization by PBS<sub>1</sub> and PBS<sub>2</sub>, and collected by BPD<sub>2</sub> and BPD<sub>3</sub>, respectively. Finally, the signals collected by data acquisition card (DAQ) were transferred to the workstation containing central processing unit (CPU) and graphics processing unit (GPU) for data processing. Note that the MCF was connected to the optical path via a fan-in-fan-out (FIFO) module and an optical switch (OS).

To achieve high-spatial-resolution 2D shape sensing with a narrow sweep range, i.e.,  $\Delta\lambda$ =4 nm, a novel wavelength shift demodulation method, i.e., adaptive spectrum method (ASM), was proposed and demonstrated, as shown in Fig. 2. Firstly, the collected reference (Ref.) and measurement (Mea.) signals were transformed from the frequency-domain to spatial-domain through fast Fourier transform (FFT). Note that the Ref. signal was collected from the MCF in a straight state, while the Mea. signal was collected in a bent state. Then, the obtained distance-domain signal was divided into multiple sensing sections through a sliding window with a width of N, i.e., N = 10. Each sliding window was padded with zero to a width of 4096, i.e., M = 4096, to improve spectral resolution. Here, the sensing spatial resolution (SR) could be given by

$$SR = N \cdot \frac{c}{2n\Delta\lambda} \tag{1}$$

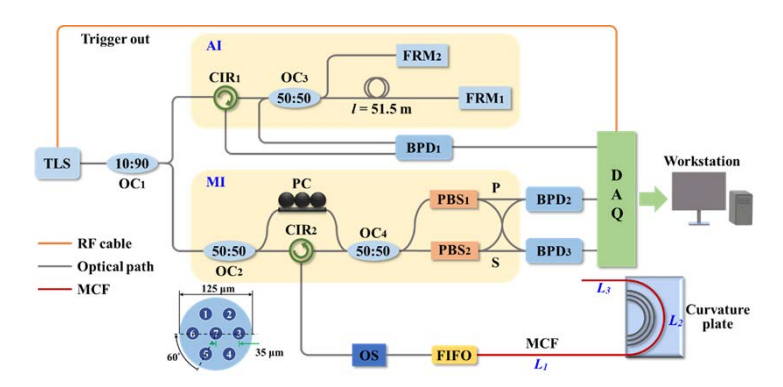


**Fig. 1.** Experimental setup for 2D shape sensing using optical frequency domain reflectometry (OFDR) with multi-core fiber (MCF). TLS: tunable laser source; OC: optical coupler; CIR: circulator; FRM: Faraday rotating mirror; PC: polarization controller; PBS: polarization beam splitter; BPD: balanced photodetector; DAQ: data acquisition card; OS: optical switch; FIFO: fan-in-fan-out. Inset: schematic diagram of MCF end face. Note that a MCF was divided into a initial zero-strain section, middle strain section, and rear zero-strain section, i.e.,  $L_1$ ,  $L_2$ , and  $L_3$ .

where c was the light velocity in vacuum, n was the refractive index of the MCF. Thus, the SR is calculated to 2.1 mm, i.e., SR = 2.1 mm. Subsequently, inverse FFT (IFFT) was performed to back to the frequency-domain to obtain the whole Ref. and Mea. spectrum. At this time, a section of local Ref. spectrum (LRS) with a spectrum length of  $\lambda_{LRS}$  was selected from the whole Ref. spectrum (WRS). Meanwhile, a section of local Mea. spectrum (LMS) with the same spectrum length as the LRS was slid with a wavelength gap of 0.00390 nm, i.e.,  $\lambda_{gap} = 0.00390$  nm within the sweep range from the whole Mea. spectrum (WMS) to match the LRS. The wavelength gap was calculated by  $\lambda_{gap} = m \cdot \Delta \lambda/M$ , where the gap contained 4 data points, i.e., m = 4. Then the normalized similarity, i.e.,  $S_i$ (i = 1, 2, ...n), between the LRS and the extracted LMSs, i.e., LMS<sub>1</sub>, LMS<sub>2</sub>, ..., LMS<sub>n</sub>, could be given by

$$S_i = \frac{\sum (LRS \cdot LMS_i)}{norm(LRS) \cdot norm(LMS_i)}$$
 (2)

where *norm* represented the Euclidean norm calculation. Finally, the maximum similarity, i.e.,  $S_{max}$ , and the number of relative position deviation, i.e.,  $\Delta d$ , between the Ref. and Mea. signal was calculated using the function of  $arg\ max$ , which could be expressed by

$$[S_{max}, \Delta d] = arg\{max(S_1, S_2, \dots, S_n)\}$$
(3)

and the original wavelength shift, i.e.,  $\delta\lambda$ , was calculated based on  $\lambda_{gap}$  and  $\Delta d$ .

In addition, the median filter was used to eliminate a few wavelength shift error points caused by large strain and narrow sweep range and enhance signal smoothness, which was given by

$$Filter(\delta \lambda_i) = Median(\delta \lambda_{i-D}, \ \delta \lambda_{i-D+1}, \ \dots, \ \delta \lambda_{i+D})$$
 (4)

where D represents the window width of the median filter, which is set to 2 in this work.

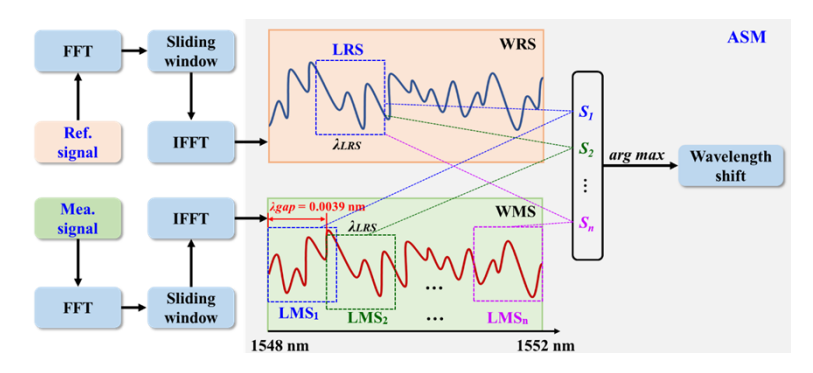


**Fig. 2.** Flow chart of wavelength shift demodulation for shape sensing based on OFDR using adaptive spectrum method (ASM). Ref. signal: reference signal; Mea. signal: measurement signal; FFT: fast Fourier transformation; IFFT: inverse FFT; WRS: whole Ref. spectrum; LRS: local Ref. spectrum; WMS: whole Mea. spectrum; LMS: local Mea. spectrum;  $S_i(i = 1, 2, ..., n)$ : normalized similarity between the LRS and LMS<sub>1</sub>, LMS<sub>2</sub>, ..., LMS<sub>n</sub>.

## 3. Experimental results and discussion

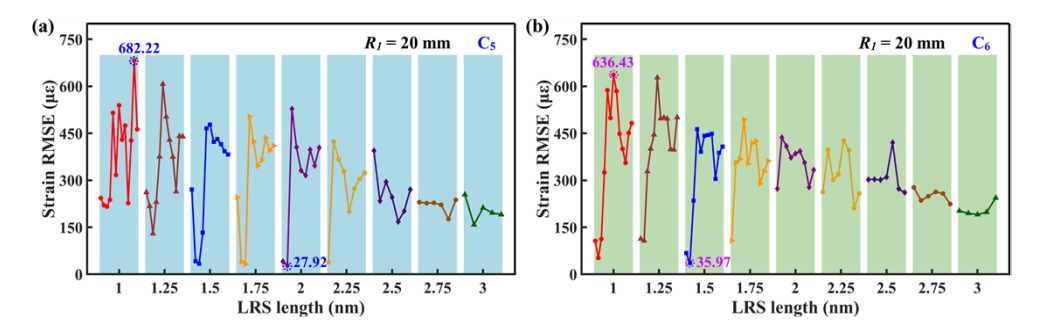
To verify the proposed method, i.e., ASM, the 2D shape sensing property of MCF was investigated. Note that the combination of  $Core_5$  ( $C_5$ ) and  $Core_6$  ( $C_6$ ), i.e.,  $C_{56}$ , was employed to reconstruct the 2D shape, as shown in the inset of Fig. 1. It is known that when the spectrum length of LRS was too large or too small, the similarity between spectra decreases significantly under large strain, i.e., minimum curvature radius [19,20]. The effect of LRS spectrum length on the root-mean-square error (RMSE) of demodulated strain for  $C_5$  and  $C_6$  at a curvature radius of 20 mm, i.e.,  $R_1 = 20$  mm, was studied, when the LRS spectrum length was increased from 1.00 to 3.00 nm in steps of 0.25 nm, i.e., 1.00, 1.25, 1.50, 1.75, 2.00, 2.25, 2.50, 2.75, and 3.00 nm. Therefore, the strain RMSEs were calculated for different LRS wavelength ranges under the afore-mentioned local spectrum lengths. Taking the LRS spectrum length of 2.00 nm as an example, the wavelength ranges within the TLS sweep range were 1548.00–1550.00, 1548.25–1550.25, 1548.50–1550.50, 1548.75–1550.75, 1549.00–1551.00, 1549.25–1551.25, 1549.50–1551.50, 1549.75–1551.75, and 1550.00–1552.00 nm, respectively, as shown in Table 1.

Table 1. The calculated RMSE for C<sub>5</sub> and C<sub>6</sub> in different wavelength ranges at local spectral lengths of 2.00 nm and 1.50 nm, respectively

C <sub>5</sub>	2.00 nm	Wavelength range	1548.00– 1550.00	1548.25- 1550.25	1548.50– 1550.50	1548.75– 1550.75	1549.00– 1551.00	1549.25– 1551.25
		RMSE	40.90	27.92	527.82	405.52	330.10	315.85
		Wavelength range	1549.50– 1551.50	1549.75– 1551.75	1550.00- 1552.00	\	\	\
		RMSE	397.95	346.85	404.39	\	\	\
	1.50 nm	Wavelength range	1548.00– 1549.50	1548.25- 1549.75	1548.50– 1550.00	1548.75– 1550.25	1549.00– 1550.50	1549.25– 1550.75
C <sub>6</sub>		RMSE	67.46	35.97	234.59	463.14	391.43	441.69
		Wavelength range	1549.50– 1551.00	1549.75– 1551.25	1550.00– 1551.50	1550.25– 1551.75	1550.50– 1552.00	\
		RMSE	444.69	448.89	304.21	387.77	407.59	\

Then the corresponding calculated RMSEs were 40.90, 27.92, 527.82, 405.52, 330.10, 315.85, 397.95, 346.85, and 404.39  $\mu\epsilon$ , respectively, as shown by the purple scatters in Fig. 3(a). Consequently, the maximum and minimum RMSEs for  $C_5$  at a LRS spectrum length of 2.00

nm were 527.82 and 27.92  $\mu\epsilon$ , corresponding to wavelength ranges of 1548.50–1550.50 and 1548.25–1550.25 nm, respectively. In addition, the maximum RMSE was 682.22  $\mu\epsilon$  at a LRS length of 1.00 nm, corresponding to a wavelength range of 1550.75–1551.75 nm. Therefore, the optimal LRS length and wavelength range of  $C_5$ , i.e., minimum strain RMSE, were 2.00 nm and 1548.25–1550.25 nm, respectively. Similarly, the strain RMSEs of  $C_6$  at above-mentioned LRS length and wavelength ranges were also calculated. As shown in Fig. 3(b) and Table 1, the minimum strain RMSE of  $C_6$  was 35.97  $\mu\epsilon$ , corresponding to LRS length and wavelength range of 1.50 nm and 1548.25–1549.75 nm, respectively.



**Fig. 3.** Calculated root mean square error (RMSE) of demodulated strain for  $C_5$  and  $C_6$  at a curvature radius of 20 mm, i.e.,  $R_1 = 20$  mm, when the LRS spectrum length was increased from 1.00 to 3.00 nm in steps of 0.25 nm. Note that the minimum strain RMSEs of  $C_5$  and  $C_6$  were 27.92 and 35.97 με, respectively, corresponding to LRS length and wavelength range of 2.00 and 1.50 nm, and 1548.25–1550.25 and 1548.25–1549.75 nm, respectively.

Then the normalized similarity was also compared at a curvature radius of 20 mm, i.e.,  $R_1 = 20$ mm, using the traditional method (TM) and ASM. Note that a 50 cm long MCF was divided into initial zero-strain section, middle strain section, and rear zero-strain section, i.e.,  $L_1$ ,  $L_2$ , and  $L_3$ , with corresponding lengths of 30.00, 6.28 and 13.72 cm, respectively, as depicted in Fig. 1. As shown in Figs. 4(a) and 4(b), the normalized similarity calculated using TM for  $C_5$  and  $C_6$ remained at a high level in the initial zero-strain section, i.e.,  $L_1$ . As is well known, the larger the normalized similarity, the more similar the Mea. spectrum is to the Ref. spectrum. Obviously, the strain in the  $L_1$  for  $C_5$  and  $C_6$  was correctly demodulated using TM, as shown in Figs. 5(a) and 5(b). However, the average normalized similarity of  $C_5$  and  $C_6$  in  $L_2$  was deteriorated to 0.514 and 0.502, respectively, due to the generation of new spectra in Mea. signal [21]. When the curvature radius was 20 mm, the strain signal was completely submerged in noise, as shown by the red curves in Figs. 5(a) and 5(b). On the contrary, the average normalized similarity in  $L_2$  for C<sub>5</sub> was improved from 0.514 to 0.816 using ASM under the LRS spectrum length of 2 nm and wavelength range of 1548.25–1550.25 nm, as shown in Fig. 4(c). And the average normalized similarity in  $L_2$  for  $C_6$  was also improved to 0.834 under the LRS spectrum length of 1.5 nm and wavelength range of 1548.25–1549.75 nm, as shown in Fig. 4(d). Obviously, the strains in  $L_2$ and  $L_3$  for  $C_5$  and  $C_6$  were successfully demodulated by using ASM, as shown by the red curves in Figs. 5(c) and 5(d).

Additionaly, the average normalized similarity of  $C_5$  and  $C_6$  at curvature radii of 25, 30, and 50 mm were also calculated and compared using TM and ASM, as shown in Table 2. The average normalized similarity of  $C_5$  was improved from 0.578, 0.606, and 0.716 to 0.872, 0.865, and 0.889, respectively, while that of  $C_6$  was improved from 0.521, 0.562, and 0.651 to 0.828, 0.836, and 0.860, respectively. Moreover, the strains of  $C_5$  and  $C_6$  were also demodulated using TM and ASM at curvature radii of 25, 30, and 50 mm, respectively. Under the same curvature radius, the strain error points in  $L_2$  of  $C_6$  demodulated using TM were more than those of  $C_5$ . Compared with TM, the random noise and strain error points in  $L_2$  were effectively eliminated by using

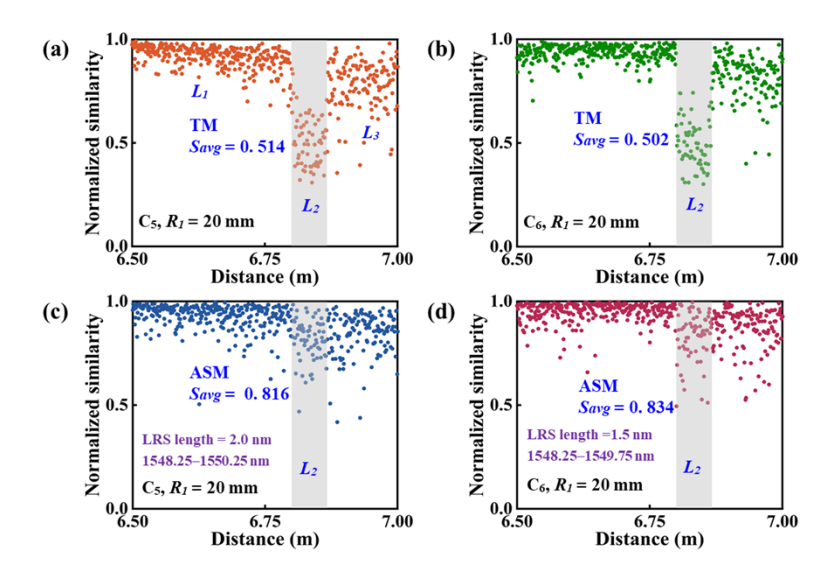


**Fig. 4.** Calculated normalized similarity of  $C_5$  and  $C_6$  in initial zero-strain section, middle strain section, and rear zero-strain section, i.e.,  $L_1$ ,  $L_2$ , and  $L_3$ , using the (a-b) traditional method (TM) and (c-d) ASM at a curvature radius of 20 mm, i.e.,  $R_1 = 20$  mm.

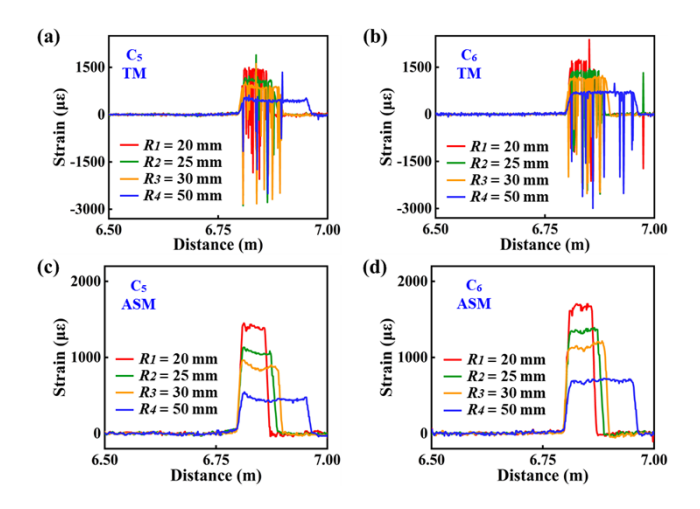


**Fig. 5.** Strain distribution of  $C_5$  and  $C_6$  using (a-b) TM and (c-d) ASM at curvature radii of 20, 25, 30 and 50 mm, respectively. Note that the spatial resolution was 2.1 mm.

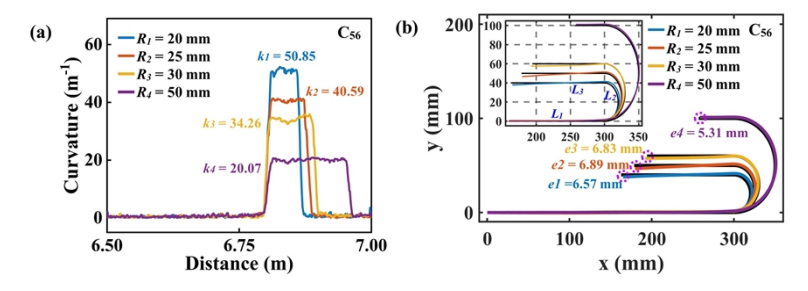
ASM based on the optimal LRS length and wavelength range of different fiber cores, as shown in Figs. 5(c) and 5(d). These results indicated that the strain signal could be accurately recovered and demodulated from the noise by using ASM with narrow sweep range.

Furthermore, the curvatures were derived using apparent curvature vector method [22] with  $C_{56}$  based on afore-obtained strains in Figs. 5(c) and 5(d). As shown in Fig. 6(a), the calculated average curvatures were 50.85, 40.59, 34.26, and 20.07 m<sup>-1</sup>, respectively, which were in good agreement with the applied curvature radii, i.e., 20, 25, 30, and 50 mm. The reconstructed 2D shapes based on Bishop frame also agreed well with the designed curvature radii, as shown in Fig. 6(b). Two methods, i.e., end position error and segmentation error, were adopted to fully evaluate the reconstruction error. Firstly, the end position reconstruction error was defined as the

Table 2. The calculated average normalized similarity of  $C_5$  and  $C_6$  in the middle strain section using TM and ASM at curvature radii of 20, 25, 30, and 50 mm, respectively

Core	Method	$R_1 = 20 \mathrm{mm}$	$R_2 = 25 \text{ mm}$	$R_3 = 30 \mathrm{mm}$	$R_4 = 50 \text{mm}$
C <sub>5</sub>	TM	0.514	0.578	0.606	0.716
CS	ASM	0.816	0.872	0.865	0.889
C <sub>6</sub>	TM	0.502	0.521	0.562	0.651
C <sub>6</sub>	ASM	0.834	0.828	0.836	0.860

position deviation between the reconstructed and theoretical position of 50 cm long MCF. As shown in Fig. 6(b), the reconstruction errors of the end position were 6.57, 6.89, 6.83 and 5.31 mm at curvature radii of 20, 25, 30, and 50 mm, respectively. Then the average position deviation between each theoretical and reconstructed coordinate of  $L_1$ ,  $L_2$ , and  $L_3$  was calculated separately. As shown in Table 3, the reconstruction error of  $L_1$  was the smallest at different curvature radii due to its zero strain. The reconstruction error of  $L_2$  was deteriorated to 4.64 mm at a curvature radius of 20 mm. Compared with  $L_1$  in the zero-strain region, the reconstruction error of  $L_3$  was noticeably larger. This was because the  $L_1$  section was fixed in a straight position on the platform, whereas the  $L_3$  section was movable, introducing placement deviations. Additionally, the cumulative reconstruction errors along the sensing fiber further increased the error in the  $L_3$  section.



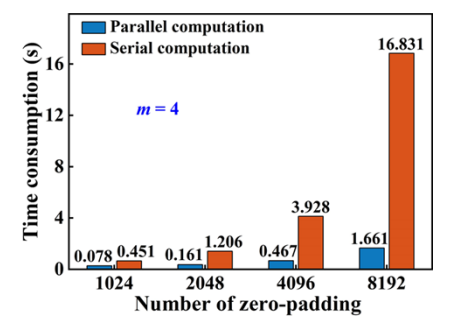
**Fig. 6.** (a) Calculated curvature and (b) reconstructed 2D shapes with curvature radii of 20, 25, 30, and 50 mm, respectively based on  $C_{56}$ . Note that  $C_{56}$  is the combination of  $Core_5$  and  $Core_6$ .

Table 3. The average reconstruction errors of  $L_1$ ,  $L_2$ , and  $L_3$  at curvature radii of 20, 25, 30, and 50 mm, respectively

Radius Segment	$R_1 = 20 \mathrm{mm}$	$R_2 = 25 \text{ mm}$	$R_3 = 30 \text{mm}$	$R_4 = 50$ mm
$L_1$	0.21 mm	0.24 mm	0.41 mm	0.18 mm
$L_2$	4.64 mm	2.64 mm	1.61 mm	2.86 mm
<i>L</i> <sub>3</sub>	2.27 mm	2.94 mm	3.05 mm	1.68 mm

In addition, the time consumption of the proposed method, i.e., ASM, was dependent on the size of zero-padding and gap length of LRS. Here, the time consumption of using CPU serial processing and graphics processing unit (GPU) parallel processing under different number of zero-padding was compared, with the LMS gap length consistently maintained at 4 data points. Note that the configurations of the CPU and GPU were the same as those in the literature [18], the serial and parallel computing were executed in MATLAB and CUDA toolkit, respectively.

Whether it was parallel or serial processing, the time consumption increased with the increasing zero-padding size, as illustrated in Fig. 7. Compared with the time consumption of 0.451, 1.206, 3.928, and 16.831 s for serial computing, the time consumption of parallel computing was reduced to 0.078, 0.161, 0.467, and 1.661 s under the size of zero-padding of 1024, 2048, 4096, and 8192. These zero-padding sizes correspond to wavelentgth gaps was 0.01560, 0.00780, 0.00390, and 0.00195 nm, respectively. Thus, the time consumption of the ASM could be reduced by a factor of 8.4 using GPU under the zero-padding size of 4096 and wavelength gap of 0.00390 nm.



**Fig. 7.** Comparison of time consumption for ASM using parallel and serial computing under the number of zero-padding of 1024, 2048, 4096, and 8192, respectively. Note that the gap length of LMS contained 4 data points.

# 4. Conclusion

In conclusion, what we believe to be a novel wavelength shift OFDR demodulation method, i.e., ASM, was proposed for high-spatial-resolution 2D shape sensing with a narrow sweep range. The minimum strain RMSEs of  $C_5$  and  $C_6$  were calculated to 27.92 and 35.97  $\mu$ E, corresponding to LRS spectrum length and wavelength range of 2.00 nm and 1548.25–1550.25 nm, 1.50 nm and 1548.25–1549.75 nm, respectively. The average normalized similarity of  $C_5$  was improved from 0.514, 0.578, 0.606, and 0.716 to 0.816, 0.872, 0.865, and 0.889 by using ASM, while that of  $C_6$  was improved from 0.502, 0.521, 0.562, and 0.651 to 0.834, 0.828, 0.836, and 0.860, respectively, at curvature radii of 20, 25, 30, and 50 mm, respectively. Compared with TM, the random noise and strain error points in  $L_2$ , i.e., strain region, was effectively eliminated by using ASM. Moreover, the reconstruction errors of the end position were 6.57, 6.89, 6.83 and 5.31 mm at curvature radii of 20, 25, 30, and 50 mm, respectively, and the average position deviation between each theoretical and reconstructed coordinate of  $L_1$ ,  $L_2$ , and  $L_3$  were calculated separately. Finally, the GPU's parallel processing capability was utilized to perform the ASM, and the time consumption was reduced by 8.4 times under the zero-padding size of 4096 and wavelength gap of 0.00390 nm.

**Funding.** National Key Research and Development Program of China (2023YFB3209500); National Natural Science Foundation of China (U22A2088, 62375178, 62222510, 62405196); Shenzhen Science and Technology Program (JCYJ20220818095800001, JCYJ20241202124226032); LingChuang Research Project of China National Nuclear Corporation (CNNC-LCKY-202265); China Postdoctoral Science Foundation (2024M752106, 2024M752107, GZC20231715, GZC20231719).

**Disclosures.** The authors declare no conflicts of interest.

**Data availability.** Data underlying the results explained in this paper are not publicly available at this time but may be obtained from the authors upon reasonable request.

### References

 J. M. Lopez-Higuera, L. R. Cobo, A. Quintela Incera, et al., "Fiber Optic Sensors in Structural Health Monitoring," J. Lightwave Technol. 29(4), 587–608 (2011).

- Y. Tian, H. Dang, W. Liu, et al., "Structure shape measurement method based on an optical fiber shape sensor," Meas. Sci. Technol. 34(8), 085102 (2023).
- 3. M. Gherlone, P. Cerracchio, M. Mattone, *et al.*, "Shape sensing methods: Review and experimental comparison on a wing-shaped plate," Prog. Aerosp. Sci. **99**, 14–26 (2018).
- J. Francoeur, A. Roberge, P. Lorre, et al., "Optical frequency domain reflectometry shape sensing using an extruded optical fiber triplet for intra-arterial guidance," Opt. Express 31(1), 396–410 (2023).
- A. Svecic, J. Francoeur, G. Soulez, et al., "Shape and Flow Sensing in Arterial Image Guidance From UV Exposed Optical Fibers Based on Spatio-Temporal Networks," IEEE Trans. Biomed. Eng. 70(5), 1692–1703 (2023).
- I. Floris, J. M. Adam, P. A. Calderón, et al., "Fiber Optic Shape Sensors: A comprehensive review," Opt. Lasers Eng. 139, 106508 (2021).
- H. Moon, J. Jeong, S. Kang, et al., "Fiber-Bragg-grating-based ultrathin shape sensors displaying single-channel sweeping for minimally invasive surgery," Opt. Lasers Eng. 59, 50–55 (2014).
- L. Szostkiewicz, M. A. Soto, Z. Yang, et al., "High-resolution distributed shape sensing using phase-sensitive optical time-domain reflectometry and multicore fibers," Opt. Express 27(15), 20763–20773 (2019).
- Z. Zhao, M. A. Soto, M. Tang, et al., "Distributed shape sensing using Brillouin scattering in multi-core fibers," Opt. Express 24(22), 25211–25223 (2016).
- Y. Meng, C. Fu, C. Du, et al., "Shape Sensing Using Two Outer Cores of Multicore Fiber and Optical Frequency Domain Reflectometer," J. Lightwave Technol. 39(20), 6624–6630 (2021).
- C. Fu, S. Xiao, Y. Meng, et al., "OFDR shape sensor based on a femtosecond-laser-inscribed weak fiber Bragg grating array in a multicore fiber," Opt. Lett. 49(5), 1273–1276 (2024).
- Y. Meng, R. Sui, W. Liang, et al., "Multicore Fiber Shape Sensing Based on Optical Frequency Domain Reflectometry Parallel Measurements," J. Lightwave Technol. 42(10), 3909–3917 (2024).
- 13. K. Liu, G. Yin, Z. Zhang, *et al.*, "Sub-millimeter resolution and high-precision phi-OFDR using a complex-domain denoising method," Opt. Lett. **49**(1), 29–32 (2024).
- Y. Tian, J. Cui, Z. Xu, et al., "Generalized Cross-Correlation Strain Demodulation Method Based on Local Similar Spectral Scanning," Sensors 22(14), 5378 (2022).
- 15. C. Shao, G. Yin, L. Lv, *et al.*, "OFDR with local spectrum matching method for optical fiber shape sensing," Appl. Phys. Express **12**(8), 082010 (2019).
- S. Li, Q. Li, Z. Ding, et al., "Twist compensated, high accuracy and dynamic fiber optic shape sensing based on phase demodulation in optical frequency domain reflectometry," Mech. Syst. Signal Process. 216, 111462 (2024).
- 17. Q. Bai, G. Yang, C. Liang, *et al.*, "Accuracy improvement of two-dimensional shape reconstruction based on OFDR using first-order differential local filtering," Opt. Express **32**(11), 19006–19018 (2024).
- R. Shan, Y. Meng, H. Zhong, et al., "Fast Shape Reconstruction Based on GPU Parallel Computation in Optical Frequency Domain Reflectometry," IEEE Sens. J. 24(21), 34591–34597 (2024).
- K. Feng, J. Cui, D. Jiang, et al., "Improvement of the strain measurable range of an OFDR based on local similar characteristics of a Rayleigh scattering spectrum," Opt. Lett. 43(14), 3293–3296 (2018).
- K. Feng, J. Cui, Y. Jin, et al., "Enhancement of the Performance and Data Processing Rate of an Optical Frequency Domain Reflectometer Distributed Sensing System Using A Limited Swept Wavelength Range," Sensors 18(10), 3480 (2018).
- 21. Y. Gan, H. Cheng, H. Jiang, *et al.*, "Research on the OFDR strain measurement method based on similarity features of dual-segment RSS," Opt. Express **32**(15), 26640–26652 (2024).
- C. Fu, Y. Meng, L. Chen, et al., "High-spatial-resolution phi-OFDR shape sensor based on multicore optical fiber with femtosecond-laser-induced permanent scatter arrays," Opt. Lett. 48(12), 3219–3222 (2023).